RSC Advances

PAPER

View Article Online
View Journal | View Issue

Cite this: *RSC Adv.*, 2017, **7**, 14910

One-pot hydrothermal synthesis of novel 3D starfish-like δ-MnO_2 nanosheets on carbon fiber paper for high-performance supercapacitors†

Bin Xu,[a] Lin Yu,*[a] Ming Sun,[a] Fei Ye,[a] Yuanhong Zhong,[a] Gao Cheng,[a] Hui Wang[a] and Yuliang Mai[bc]

Received 18th January 2017
Accepted 1st March 2017

DOI: 10.1039/c7ra00787f

rsc.li/rsc-advances

Novel 3D starfish-like δ-MnO_2 nanosheets with a hierarchical nanostructure supported on carbon fiber paper were synthesized through a facile hydrothermal method. These unique interconnected starfish-like nanosheets acting as a binder-free electrode exhibit a high specific capacitance (336 F g^{-1} at a current density of 1 A g^{-1}), good rate capability (57.1% retention when the current density increases from 1 to 20 A g^{-1}), and extraordinary electrochemical cycling characteristics (125.3% retention of the initial specific capacitance after 7000 cycles at a high current density of 10 A g^{-1}). The impressive electrochemical performance of this starfish-like δ-MnO_2 electrode was mainly attributed to its distinctive microstructure and large BET surface area, which could highly shorten the transport path of the ion/electron and provide more electroactive sites for electrochemical reaction. Therefore, it can be expected that this unique starfish-like δ-MnO_2 electrode may have great promise for application in supercapacitors.

Introduction

Along with the rapid development of the economy, there is an urgent requirement for efficient, clean, and renewable sources of energy, as well as new technologies associated with energy conversion and storage devices due to the enormous consumption of fossil fuels and the increasing pollution problems of the environment.[1–4] As one of the most promising energy storage/conversion devices, electrochemical capacitors (ECS), namely supercapacitors (SCs), have attracted extensive attention due to their high power density, rapid charge–discharge rate, long lifecycle, safe operation, and bridging the power/energy gap between traditional dielectric capacitors and batteries.[5–8] These favorable characteristics are beneficial for practical applications of supercapacitors in the future. They can either directly serve as a stand-alone energy supply device for many applications or couple with other energy conversion devices such as fuel cells to serve as an efficient energy storage system for continuous power supply.[9–11] Generally, supercapacitors can be classified into two types according to their underlying charge storage mechanisms, electric double-layer capacitors (EDLCs) and pseudocapacitors. For EDLCs materials, *e.g.*, carbonaceous materials, they store energy *via* the electrostatic storage of charge at the interface between electrode and electrolyte.[12,13] Unlike EDLCs, pseudocapacitor materials, based on conducting polymers or transition metal oxides, exploit the reversible Faradaic reactions that happen in the internal of electrode materials, and thus are more effective because they can provide much high specific capacitance and energy density when compared to EDLCs.[4,14,15]

Among various transition metal oxides, MnO_2 is one kind of attractive pseudocapacitive materials due to its high theoretical capacity (1370 F g^{-1}), environmental friendliness, low cost, and abundant resource.[16–22] Moreover, the unique physical and chemical properties of MnO_2 result in an extensive applications including catalysis,[23] magnetic materials,[24] lithium ion batteries,[25] and supercapacitors.[26] However, the poor electrical conductivity and low structural stability of MnO_2 restrict their practical application for supercapacitors. To address these problems, some solutions have been gradually proposed. For one thing, studies on incorporating MnO_2 nanostructures with carbon-based materials or conducting polymers to improve the electrical conductivity, charge–discharge rate and cycling ability have been carried out.[27–29] For example, Wang *et al.* have successfully synthesized MnO_2/carbon nanotubes nanocomposites *via* three-step method, and the composites exhibited a maximum specific capacitance of 348 F g^{-1} at a scan rate

[a]*Key Laboratory of Clean Chemistry Technology of Guangdong Regular Higher Education Institutions, School of Chemical Engineering and Light Industry, Guangdong University of Technology, Guangzhou 510006, P. R. China. E-mail: gych@gdut.edu.cn*

[b]*Petrochemical Research Institute of Guangdong Province, Guangzhou 510006, P. R. China*

[c]*Guangdong Research Institute of Petrochemical and Fine Chemical Engineering, Guangdong Provincial Key Laboratory of Industrial Surfactant, Guangzhou 510006, P. R. China*

† Electronic supplementary information (ESI) available. See DOI: 10.1039/c7ra00787f

of 5 mV s^{-1}.[30] Wang *et al.* reported that the polypyrrole (PPy) nanofilms are grown on the mesoporous MnO_2 by chemical vapor deposition, and the MnO_2/PPy presents a high specific capacitance of 320 F g^{-1}.[31] For another, the cationic doping has been demonstrated as an effective way to enhance the conductivity of materials. Zhao *et al.* reported the rational synthesis of Cu-doped porous δ-MnO_2 which has delivered a high specific capacitance of 300 F g^{-1} at scan rate of 5 mV s^{-1}.[32] However, the challenge remains to obtain a simple and low cost preparation process and high-performance of MnO_2 electrode materials.

An effective method is to grow MnO_2 with unique nanostructures on conducting substrates as the binder-free electrodes for supercapacitors. It can not only enhance the conductivity and effective utilization of the active materials, but also avoid the complicated electrode preparation process. Among various nanostructures, 3D hierarchical structure materials, would exhibit excellent rate capabilities and long-term cycling stability, because the 3D hierarchical structures with nanoscale building blocks could realize efficient electron/ion transport and a stable structure during cycling process when compared to 1D and 2D structures.[33] The common explanation for the remarkable electrochemical performance of 3D hierarchical structures is that they could not only enlarge the contact area between the electrode and electrolyte, shorten the pathway of electrons/ions transport, and effectively facilitate ionic diffusion, but also accommodate the volume changes and maintain the stability of the hierarchical network structure during cycling process.[34] Therefore, rational synthesis of 3D hierarchical nanostructures materials on conductivity substrates is desirable.

In this work, we have developed a facile one-pot hydrothermal method for synthesis of 3D hierarchical starfish-like δ-MnO_2 nanosheet arrays on carbon fiber paper (CFP). The resulting sample morphology was of starfish-like nanostructure, which was composed of four, five, or six-rayed sea star. To the best of our knowledge, there are few reports of 3D hierarchical starfish-like δ-MnO_2 nanosheets as high-performance electrode materials for supercapacitors. Benefiting from favorable starfish structure as well as the rational design of a binder-free electrode, the starfish-like δ-MnO_2 nanosheet electrode exhibits a higher capacitance (336 F g^{-1} at a current density of 1 A g^{-1}), good rate capability (57.1% retention when current density increase from 1 to 20 A g^{-1}), and excellent cycling ability (125.3% retention after 7000 cycles).

Experimental section

Synthesis of the starfish-like δ-MnO_2 nanosheets

All the chemicals were of analytical grade and were used without further purification. Commercial CFP (approximately 1 cm × 4 cm) was purified under ultrasonic treatment in 3 M HCl aqueous solution, absolute ethanol and distilled water for 30 min, respectively. In this typical experiment, 1.5 mmol K_2SO_3 was dissolved in 20 mL distilled water to form a transparent solution, and then 10 mL/0.1 M $KMnO_4$ solution was added by drops following by a vigorous stirring at room temperature for 25 min. Subsequently, the solution was transferred into a 50 mL Teflon-lined stainless steel autoclave, and a piece of the pretreated CFP was put vertically into the autoclave. Lastly, the autoclave was heated to 120 °C and kept for 24 h. After the reaction, the autoclave was taken out, cooled to room temperature, and the CFP substrate with the active materials was taken out, ultrasonically cleaned with distilled water and ethanol, respectively, for several times, and then dried at 70 °C for 12 h. The final mass loading of the MnO_2 was around 3.2 mg cm^{-2}.

Characterization

The crystalline structure of the as-synthesized sample (scraped the powders from the CFP) was examined by X-ray diffraction diffractometer (XRD, Bruker, D8, Cu Kα, $\lambda = 1.5406$ Å). Raman scattering (RS) spectra were conducted on a dispersive Horiva Jobin Yvon LabRam HR800 Microscope, with a 633 nm laser and 24 mW laser powers. X-ray photoelectron spectroscopy (XPS) was performed on a Thermo ESCALAB 250 instrument equipped with a monochromatic Al Kα (1486.6 eV) X-ray source, and the spectra are calibrated using the carbon peak. The morphology and microstructure of the sample were characterized by scanning electron microscopy (SEM, Hitachi, S-3400N), flied emission scanning electron microscopy (FESEM, Hitachi, S-4800) and transmission electron microscopy (TEM, shimadzu, EPMA-1600). The nitrogen adsorption–desorption measurements were performed using ASAP 2000 instrument at 77 K.

Electrochemical characterization

Electrochemical properties of the samples were investigated by cyclic voltammetry (CV), galvanostatic charge–discharge (GCD) and electrochemical impedance spectra (EIS) on the electrochemical working station (CHI 660E, Chenhua, PR China) in a three-electrode cell containing 1 M Na_2SO_4 electrolyte at room temperature. The CFP with the electrochemical active materials (around 1 cm^2 in area) directly serves as the working electrode, and the platinum foil electrode and saturated calomel electrode (SEC) are used as the counter electrode and the reference electrode, respectively.

Capacitance calculation

The specific capacitance of the sample was calculated using the following equation:

$$C = I\Delta t/(m\Delta V)$$

where the C, I, Δt, m and ΔV represent the specific capacitance (F g^{-1}), discharge current density (mA), discharge time (s), the mass of the active material (mg), and the potential drop during discharge (V), respectively.

Results and discussion

Characterizations of the starfish-like δ-MnO_2 nanosheets

The XRD pattern of the as-synthesized sample was shown in Fig. 1a. It can be clearly observed that the main characteristic peaks located at 12.5°, 25.2° and 37.3° were corresponded to the (001), (002) and (−111) planes of δ-MnO_2 (JCPDS 80-1098),

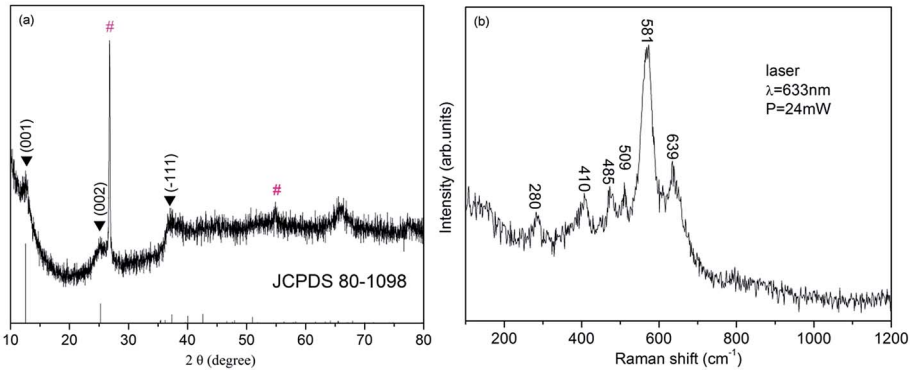

Fig. 1 (a) XRD pattern and (b) Raman spectra of the starfish-like δ-MnO_2.

respectively, and no additional peak appears, excluding the two peaks resulting from CFP (marked with '#'). The structure of the sample was further characterized by Raman spectroscopy (Fig. 1b). Six major vibrational features corresponding to δ-MnO_2 can be observed at 280, 410, 485, 509, 581 and 639 cm^{-1}. The two high-wavenumber bands at 581 and 631 cm^{-1} in the Raman spectrum were assigned to the ν_3(Mn–O) stretching vibration in the basal plane of MnO_6 sheets and the symmetric stretching vibration ν_2(Mn–O) of MnO_6 groups of a birnessite-type δ-MnO_2, respectively.[35,36] To sum up the birnessite-type δ-MnO_2 was successfully obtained.

X-ray photoelectron spectroscopy was further used to identify the surface chemical composition and oxidation state of the δ-MnO_2. As shown in Fig. 2a, the XPS signals of elements C, O and Mn could be seen in the XPS survey spectrum, illustrating the attachment of MnO_2 on the surface of carbon fiber paper (CFP). Fig. 2b shows the Mn 2p core level spectra of δ-MnO_2. Two peaks centered at 653.9 and 642.1 eV, which can be attributed to the binding energy of Mn $2p_{1/2}$ and Mn $2p_{3/2}$, respectively, and the spin-energy separation was 11.7 eV indicating presence of a large number of tetravalent Mn and a small amount of trivalent Mn. Moreover, the Mn 3s and O 1s core-level spectra were also used to more accurately confirm the oxidation state of manganese.[37] As shown in Fig. 2c, the Mn 3s core level peak of δ-MnO_2 shows peak splitting, and the peak spin-energy separation (ΔE) is 4.9 eV. According to an the linear relationship between ΔE and the oxidation state of manganese reported by Toupin *et al.*,[38] the average oxidation state of Mn was approximately of 3.8. In the case of O 1s spectra (Fig. 2d), the O 1s spectrum consists of two oxygen containing chemical bonds,

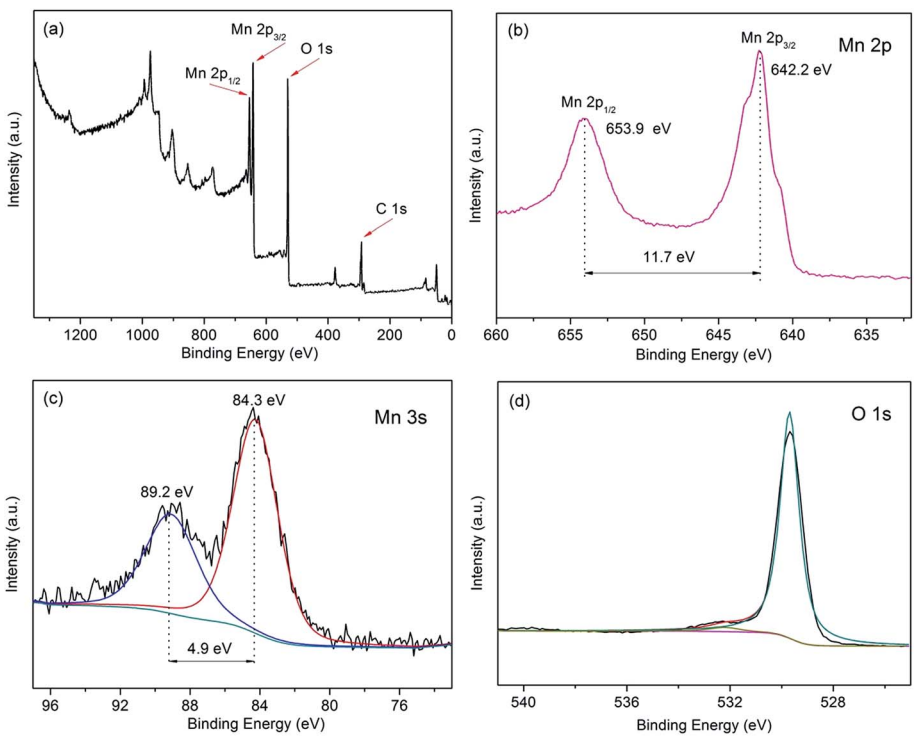

Fig. 2 XPS of the starfish-like δ-MnO_2: (a) wide scan survey, (b) Mn 2p, (c) Mn 3s, (d) O 1s.

i.e., water molecule H–O–H, and Mn–O–Mn bonds,[39] one of the strong peak centered at 529.6 eV was Mn–O–Mn bonds, and the other weak peak centered at 532.5 eV was H–O–H bond.

The morphology of the sample supported on CFP was investigated by scan electron microscope (SEM) and field emission scan electron microscope (FESEM). As shown in Fig. 3a–c, the numerous nanosheets were homogeneously covered on the skeleton of CFP, forming a highly open structure at a large scale (the material filled between carbon fiber was also the as-synthesized δ-MnO_2 nanosheets as shown in Fig. 3a). From the enlarged views (Fig. 3d), it can be seen that the δ-MnO_2 nanosheets were actually components of the starfish architecture, and the single starfish architecture was consisted of four-, five-, or six-rayed sea star. As shown in Fig. 3e and f, the overall size of an individual starfish-like δ-MnO_2 was about 500 nm, and it can be clearly seen that the thickness of the single starfish nanosheet was approximately 10–30 nm. Numerous starfish-like δ-MnO_2 nanosheets uniformly form a hierarchical 3D network structure *via* the interconnection between neighboring nanosheets and hierarchical linkage of the starfish-like δ-MnO_2 nanosheets. Such features could favour for the penetration of the electrolyte, shortening of the transport path, and accommodation the volume change during cycling process which could lead to a better electrochemical performance.[33,40]

In order to study the growth process of such hierarchical starfish-like δ-MnO_2, time-dependent experiments were carried out. As shown in Fig. S1a,† the nanoplatelet of MnO_2 was uniformly deposited on CFP with arbitrary direction at first after 1 h. With the hydrothermal time increase to 3 h, the nanoplatelet gradually grew up, and several adjacent nanoplatelets started to connect with each other to form the starfish precursor (Fig. S1b†). The faint starfish morphology could be found after 6 h as shown in Fig. S1c.† When the reaction time was prolonged to 12 h, it can be clearly seen that the starfish precursor has grown up toward 3D direction with an appearance of rough nanosheets (shown in Fig. S1d†). After 18 h, the clear starfish began to appear with several curled nanosheets as depicted in Fig. S1e.† Finally, the starfish-like δ-MnO_2 nanosheets was synthesized after 24 h (Fig. S1f†).

The microstructures of the starfish-like δ-MnO_2 nanosheets were further investigated by TEM. As shown in Fig. 4a, the starfish was composed of ultrathin nanosheets, which agrees well with the above SEM results. The ultrathin nanosheets show a rough surface and possess many pores with several nanometers in size as depicted in Fig. 4b. This unique structure can offer large surface area that would contact with the electrolyte in the fast reversible faradic redox reactions. The selected area electron diffraction (SAED) pattern (Fig. 5b inset) contains three faint continuous diffraction rings, showing the polycrystalline nature of the starfish-like δ-MnO_2.[41]

Fig. 5 shows the N_2 adsorption–desorption isotherms and pore size distribution of the starfish-like δ-MnO_2. From Fig. 6a, the isotherm can be identified as type IV due to the obvious hysteresis loop at P/P_0 of 0.45,[42] indicating the presence of mesoporous structure for the as-synthesized sample. The BET surface area of the as-prepared sample was calculated to be 47.8 $m^2\ g^{-1}$, and thus the starfish-like δ-MnO_2 may exhibit better electrochemical properties because the larger surface area could provide more electroactive sites for electrochemical reaction. Moreover, the pore size distribution of the sample was further determined by the desorption isotherm using Barrete–Joynere–Halenda (BJH) method (Fig. 5b), and the average pore diameter was approximately 5.7 nm, which is consistent with that of the TEM analysis. The pore volume is calculated as 0.08 $cm^3\ g^{-1}$ based on the isotherm. Such a relatively open structure could greatly relieve stress from the inside and provide facile pathway, ensuring the ideal electrochemical property of MnO_2 porous nanosheets.

Capacitive performances of the starfish-like δ-MnO_2 nanosheets

The capacitive performance of the starfish-like δ-MnO_2 nanosheets grown on CFP was evaluated by cyclic voltammograms (CV), galvanostatic charge–discharge (GCD), and electrochemical

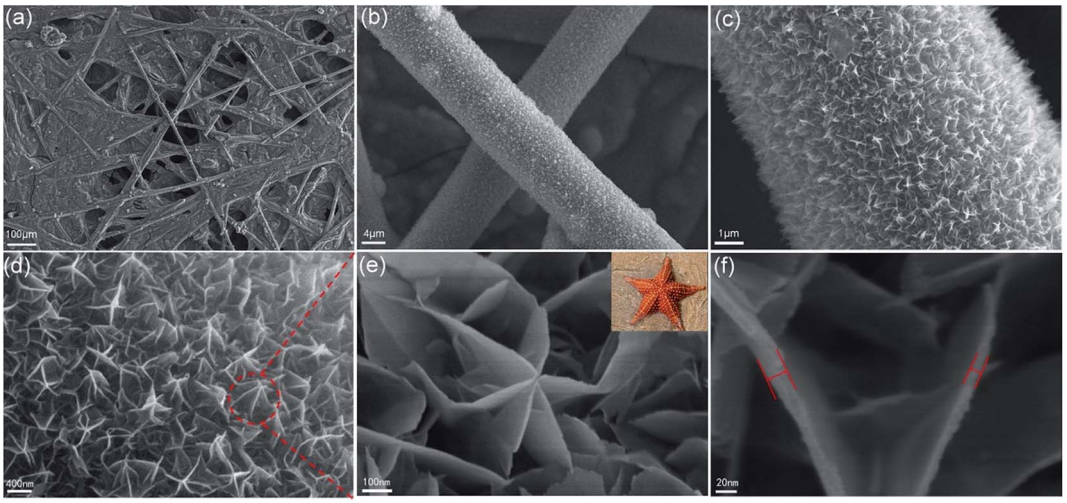

Fig. 3 (a–d) SEM and (e and f) FESEM image of the starfish-like δ-MnO_2 with different magnification. Upper-right inset in (e) is the real starfish.

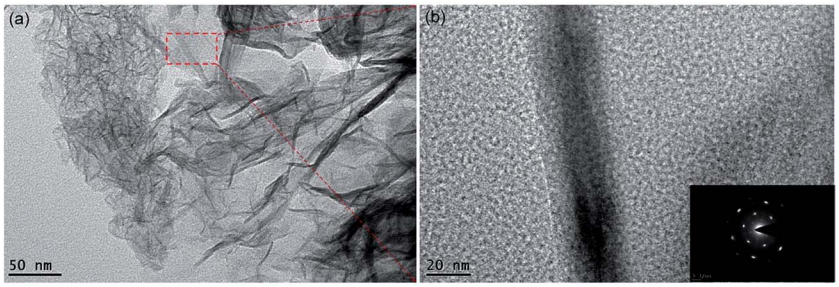

Fig. 4 (a) Low-magnification TEM images of the starfish-like δ-MnO_2 nanosheets. (b) HRTEM images of the starfish-like δ-MnO_2 nanosheets. The inset in bottom-right is the corresponding SAED pattern.

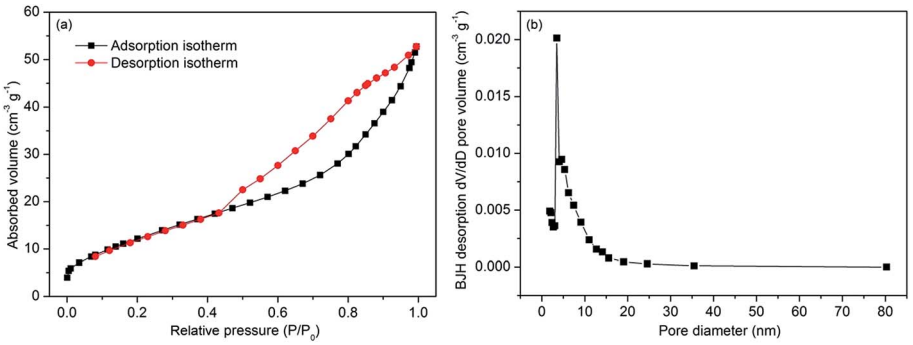

Fig. 5 N_2 adsorption–desorption isotherm (a) and pore size distribution curves (b) of the starfish-like δ-MnO_2 nanosheets.

impedance (EIS). The CV cures of the as-synthesized MnO_2 display a similar rectangular shape at various scan rates ranging from 5 to 80 mV s^{-1} (Fig. 6a), indicating an ideal capacitive performance. From Fig. 6b, the shape of the CV curves reveals the pseudocapacitive characteristics of the starfish-like δ-MnO_2 electrode, while the bare CFP was formed a straight line means that the capacitance contribution from the CFP is negligible, thus the capacitance contribution is all from the starfish-like δ-MnO_2 electrode. To further evaluate the capacitive, Fig. 6c showing the GCD profiles of the starfish-like δ-MnO_2 electrode at the current density from 1 to 20 A g^{-1} in the voltage window of 0–1 V. Obviously, the GCD profiles are more symmetric at different current density, implying that the starfish-like δ-MnO_2 electrode has higher charge–discharge coulombic efficiency and lower polarization. The specific capacitance of the MnO_2 electrode as a function of current density calculated by the GCD curves was shown in Fig. 6d. The specific capacitances of the starfish-like δ-MnO_2 electrode were 336, 314, 300, 280, and 192 F g^{-1} respectively, at various current density ranges from 1 to 20 A g^{-1}. As we know, ions could penetrate into the inner-structure of the electrode material and make full use of the active material at lower current density, but there is only the outer surface can be effective utilized at high current density, and thus lead to a relatively lower specific capacitance. It is noteworthy that, the specific capacitance of the starfish-like δ-MnO_2 electrode is calculated to be 336 F g^{-1}, which is much higher than many previous reported MnO_2 materials,[42,43] indicating that the highly porous structure and the high BET surface area of the MnO_2 electrode can facilitate ion transfer to the porous structure. Furthermore, the as-synthesized MnO_2 electrode retains 83.3% of its initial specific capacitance when the current density increases from 1 to 10 A g^{-1}, and there is also 57.1% retention of initial specific capacitance when the current density even increases from 1 to 20 A g^{-1}, revealing the excellent rate capability of this starfish-like MnO_2 electrode. The superior capacitive performance could be ascribed to the novel 3D hierarchical starfish-like architecture and the porous structure, as well as the abundant electroactive sites due to the large BET surface area of the starfish-like MnO_2 nanosheets, for these features could benefit the fast transition of the ion/electron and the speed of electrochemical reaction.

To further demonstrate the superiority of the as-synthesized MnO_2 electrode, the long-term stability was tested at a current density of 10 A g^{-1} for 7000 cycles, as depicted in Fig. 6e. Impressively, there is a great increase (~25.3%) of the initial capacitance after 7000 continuous charge–discharge cycles and the specific capacitance reaches up to 351 F g^{-1}. This fascinating cycling behavior may be because of the activation process of the electrode at the initial period of constant current charge–discharge cycling test. Meanwhile, the interesting behavior demonstrates the extraordinary cycling performance of the starfish-like δ-MnO_2, and which is significantly beneficial for practical applications in supercapacitors.[39,44] The charge–discharge curves of the initial and last 5 cycles were shown in the inset of Fig. 6e. It can be seen that the charge and its corresponding discharge curve were still symmetric, implying that there may be no obviously structural change for the starfish-like

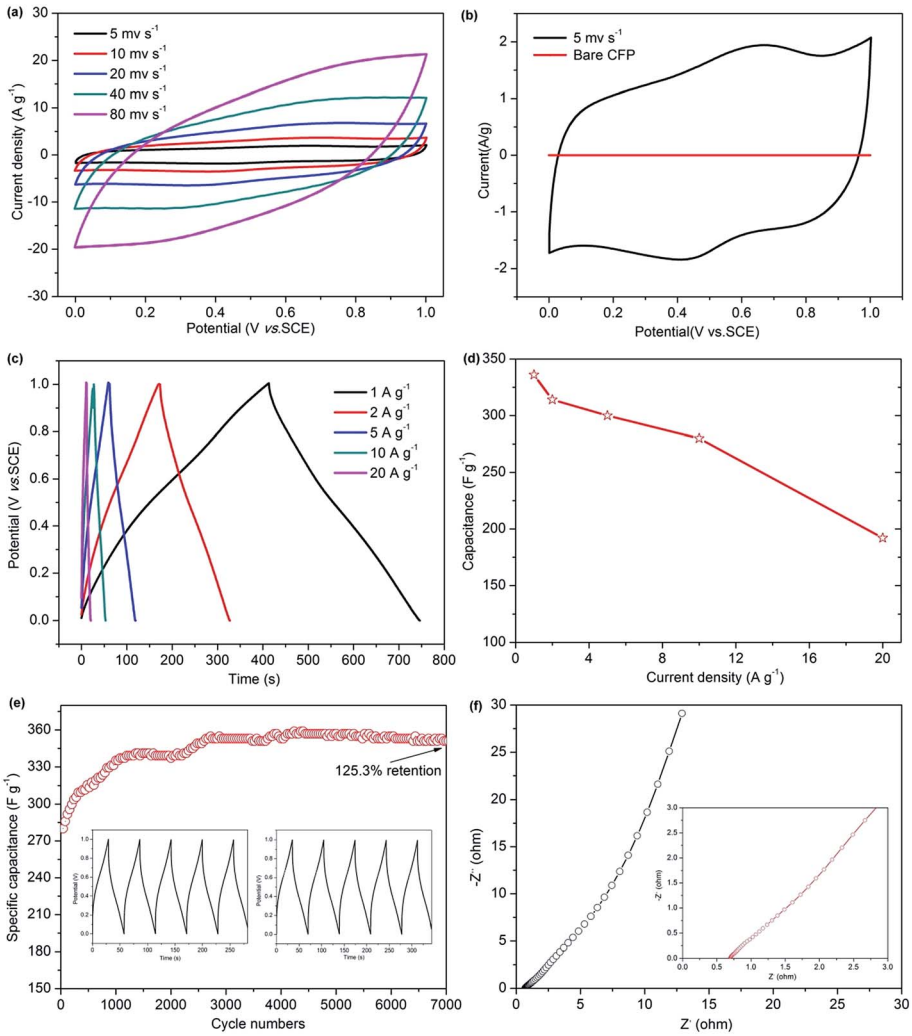

Fig. 6 The electrochemical performances of the starfish-like MnO_2 nanosheets; (a) CV curves, (b) CV curves of the starfish-like δ-MnO_2 nanosheets electrode and bare carbon fiber paper (CFP) at a scan rate of 5 mV s^{-1}, (c) galvanostatic charge–discharge curves, (d) specific capacitance as a function of the current density based on the respective charge–discharge curves, (e) cycling stability at a constant current of 10 A g^{-1}. The inset shows the cycling performance curves of the initial and last 5 cycles, respectively. (f) EIS plots at open circuit potential in the frequency range from 0.01 Hz to 100 kHz. The inset shows its magnification plot.

δ-MnO_2 electrode during the cycling process. To gain further insight into the transport kinetic of the electrochemical behavior, the EIS spectrum of the starfish-like δ-MnO_2 electrode was obtained in the frequency range from 0.01 Hz to 100 kHz at open circuit potential. As shown in Fig. 6f, the equivalent series resistance (ESR) of the starfish-like δ-MnO_2 electrode was evaluated to be 0.69 Ω, which is much smaller than that of previously reported MnO_2 electrode,[32] indicating a lower bulk resistance of the this MnO_2 electrode. Moreover, it is interesting and noteworthy that the Nyquist plots of the starfish-like δ-MnO_2 electrode do not show semicircle in the high frequency region. It suggests that it has much lower charge transfer resistances, which could greatly enlarge the rate capability of the electrode.[45,46] In general, the EIS results clearly demonstrate that the starfish-like δ-MnO_2 electrode exhibits favorable charge–discharge kinetics and good electrical conductivity, and thus shows excellent electrochemical performance.

Conclusion

In summary, the starfish-like δ-MnO_2 nanosheets was synthesized on carbon fiber paper. The MnO_2 electrode shows an excellent electrochemical performance, with a high specific capacitance of 336 F g^{-1} at a current density of 1 A g^{-1}, and an extraordinary cycling stability with 125.3% retains of initial specific capacitance at current density of 10 A g^{-1}, and an outstanding rate capability with 57.1% retains of the initial specific capacitance when the current density increases from 1 to 20 A g^{-1}. This excellent electrochemical properties were mainly attributed to the following two factors: (1) its unique morphology of hierarchical 3D starfish-like nanosheets that can be beneficial for fast and efficient ionic diffusion, electron transfer, and better accommodation to the volume change during long-term charge–discharge process; (2) its larger BET surface area that could provide abundant electroactive sites for

electrochemical reaction. All of these results suggest that the δ-MnO_2 electrode may have larger potential for future supercapacitor applications.

Acknowledgements

This work was financially supported by the National Natural Science Foundation of China (21576054), the Scientific Project of Guangdong Province (2014A010106030, 2106A010104017, 2016B020241003), the Foundation of Higher Education of Guangdong Province (2015KTSCX027).

Notes and references

1 J.-G. Wang, D. Jin, R. Zhou, C. Shen, K. Xie and B. Wei, *J. Power Sources*, 2016, **306**, 100–106.
2 S. Kong, K. Cheng, Y. Gao, T. Ouyang, K. Ye, G. Wang and D. Cao, *J. Power Sources*, 2016, **308**, 141–148.
3 Y. Xiao, Y. Lei, B. Zheng, L. Gu, Y. Wang and D. Xiao, *RSC Adv.*, 2015, **5**, 21604–21613.
4 Y. Zhang, C. Sun, P. Lu, K. Li, S. Song and D. Xue, *CrystEngComm*, 2012, **14**, 5892.
5 B. Zhu, S. Tang, S. Vongehr, H. Xie and X. Meng, *ACS Appl. Mater. Interfaces*, 2016, **8**, 4762–4770.
6 S. Liu, K. S. Hui and K. N. Hui, *ACS Appl. Mater. Interfaces*, 2016, **8**, 3258–3267.
7 W. Fu, X. Li, C. Zhao, Y. Liu, P. Zhang, J. Zhou, X. Pan and E. Xie, *Mater. Lett.*, 2015, **149**, 1–4.
8 Z. S. Wu, Y. Sun, Y. Z. Tan, S. Yang, X. Feng and K. Mullen, *J. Am. Chem. Soc.*, 2012, **134**, 19532–19535.
9 S. Bag and C. R. Raj, *J. Mater. Chem. A*, 2016, **4**, 587–595.
10 E. Frackowiak, Q. Abbas and F. Béguin, *J. Energy Chem.*, 2013, **22**, 226–240.
11 R. J. B. Martin Winter, *Chem. Rev.*, 2004, **104**, 4245–4269.
12 Y. He, W. Chen, X. Li, Z. Zhang, J. Fu, C. Zhao and E. Xie, *ACS Nano*, 2013, **7**, 174–182.
13 A. Boisset, L. Athouël, J. Jacquemin, P. Porion, T. Brousse and M. Anouti, *J. Phys. Chem. C*, 2013, **117**, 7408–7422.
14 C. Mao, S. Liu, L. Pang, Q. Sun, Y. Liu, M. Xu and Z. Lu, *RSC Adv.*, 2016, **6**, 5184–5191.
15 A. Pendashteh, J. Palma, M. Anderson and R. Marcilla, *J. Mater. Chem. A*, 2015, **3**, 16849–16859.
16 H. R. Moazami, S. S. H. Davarani, T. Yousefi and A. R. Keshtkar, *Mater. Sci. Semicond. Process.*, 2015, **30**, 682–687.
17 H. Huang, W. Zhang, Y. Fu and X. Wang, *Electrochim. Acta*, 2015, **152**, 480–488.
18 E. R. Ezeigwe, M. T. T. Tan, P. S. Khiew and C. W. Siong, *Ceram. Int.*, 2015, **41**, 11418–11427.
19 L. Coustan, A. L. Comte, T. Brousse and F. Favier, *Electrochim. Acta*, 2015, **152**, 520–529.
20 S. J. Zhu, J. Zhang, J. J. Ma, Y. X. Zhang and K. X. Yao, *J. Power Sources*, 2015, **278**, 555–561.
21 T. Wang, F. Dong and Y. X. Zhang, *Mater. Lett.*, 2016, **171**, 319–322.
22 Q. Y. Shan, B. Guan, S. J. Zhu, H. J. Zhang and Y. X. Zhang, *RSC Adv.*, 2016, **6**, 83209–83216.
23 T. Lin, L. Yu, M. Sun, G. Cheng, B. Lan and Z. Fu, *Chem. Eng. J.*, 2016, **286**, 114–121.
24 C. Luo, Z. Tian, B. Yang, L. Zhang and S. Yan, *Chem. Eng. J.*, 2013, **234**, 256–265.
25 Y. Wang, P. Ding and C. Wang, *J. Alloys Compd.*, 2016, **654**, 273–279.
26 K. Zhu, Y. Wang, J. A. Tang, H. Qiu, X. Meng, Z. Gao, G. Chen, Y. Wei and Y. Gao, *RSC Adv.*, 2016, **6**, 14819–14825.
27 M. Liu, W. W. Tjiu, J. Pan, C. Zhang, W. Gao and T. Liu, *Nanoscale*, 2014, **6**, 4233–4242.
28 P. Li, Y. Yang, E. Shi, Q. Shen, Y. Shang, S. Wu, J. Wei, K. Wang, H. Zhu, Q. Yuan, A. Cao and D. Wu, *ACS Appl. Mater. Interfaces*, 2014, **6**, 5228–5234.
29 M. Kim, Y. Hwang and J. Kim, *Phys. Chem. Chem. Phys.*, 2014, **16**, 351–361.
30 J.-W. Wang, Y. Chen and B.-Z. Chen, *J. Alloys Compd.*, 2016, **688**, 184–197.
31 N. Wang, P. Zhao, K. Liang, M. Yao, Y. Yang and W. Hu, *Chem. Eng. J.*, 2017, **307**, 105–112.
32 S. Zhao, T. Liu, M. S. Javed, W. Zeng, S. Hussain, Y. Zhang and X. Peng, *Electrochim. Acta*, 2016, **191**, 716–723.
33 X. Liang, G. Gao, G. Wu and H. Yang, *Electrochim. Acta*, 2016, **188**, 625–635.
34 Q. An, F. Lv, Q. Liu, C. Han, K. Zhao, J. Sheng, Q. Wei, M. Yan and L. Mai, *Nano Lett.*, 2014, **14**, 6250–6256.
35 J. Zhou, L. Yu, M. Sun, S. Yang, F. Ye, J. He and Z. Hao, *Ind. Eng. Chem. Res.*, 2013, **52**, 9586–9593.
36 C. Julien, *Solid State Ionics*, 2003, **159**, 345–356.
37 M. Kim and J. Kim, *ACS Appl. Mater. Interfaces*, 2014, **6**, 9036–9045.
38 T. B. Mathieu Toupin and D. Belanger, *Chem. Mater.*, 2004, **16**, 3184–3190.
39 T. B. Mathieu Toupin and D. B. langer, *Chem. Mater.*, 2002, **14**, 3946–3952.
40 L. Gao, S. Xu, C. Xue, Z. Hai, D. Sun and Y. Lu, *J. Nanopart. Res.*, 2016, **18**, 112–122.
41 T. Nguyen, M. Boudard, M. J. Carmezim and M. F. Montemor, *Electrochim. Acta*, 2016, **202**, 166–174.
42 S. Lu, D. Yan, L. Chen, G. Zhu, H. Xu and A. Yu, *Mater. Lett.*, 2016, **168**, 40–43.
43 X. Su, L. Yu, G. Cheng, H. Zhang, M. Sun and X. Zhang, *Appl. Energy*, 2015, **153**, 94–100.
44 M. Zhu, D. Meng, C. Wang and G. Diao, *ACS Appl. Mater. Interfaces*, 2013, **5**, 6030–6037.
45 P. Sivaraman, A. R. Bhattacharrya, S. P. Mishra, A. P. Thakur, K. Shashidhara and A. B. Samui, *Electrochim. Acta*, 2013, **94**, 182–191.
46 L. Yang, S. Cheng, Y. Ding, X. Zhu, Z. L. Wang and M. Liu, *Nano Lett.*, 2012, **12**, 321–325.

